Adriano *et al. Geosci. Lett. (2018) 5:2*
https://doi.org/10.1186/s40562-017-0100-9

Geoscience Letters

RESEARCH LETTER

Open Access

Tsunami source and inundation features around Sendai Coast, Japan, due to the November 22, 2016 M_w 6.9 Fukushima earthquake

Bruno Adriano[1*], Yushiro Fujii[2] and Shunichi Koshimura[1]

Abstract

The tsunami source of the 2016 Fukushima Earthquake, which was generated by a normal faulting earthquake mechanism, is estimated by inverting the tsunami waveforms that were recorded by seven tide gauge stations and two wave gauge stations along the north Pacific coast of Japan. Two fault models based on different available moment tensor solutions were employed, and their locations were constrained by using the reverse tsunami travel time from the stations to the epicenter. The comparison of the two fault slip models showed that the fault model with a strike = 49°, dip = 35°, and rake = −89° more accurately simulated the observed tsunami data. This fault model estimated a fault area of 40 km × 32 km. The largest slip was estimated as 4.66 m at a 6.09 km depth, larger slips also concentrated between depths of 6.06 and 10.68 km, and located southwest of the epicenter. Assuming a rigidity of 2.7×10^{10} N/m^2, the estimated moment magnitude was 3.35×10^{19} Nm (equivalent to $M_w = 6.95$). In addition, a comparison of nonlinear tsunami simulations using finer bathymetry around Sendai Coast verified that the above fault slip model could better reproduce the tsunami features observed at Sendai Port and its surroundings. Finally, we analyzed the nonlinear tsunami computed from our best fault slip model. Our simulations also corroborated the height of the secondary wave amplitude observed at Sendai Port, which was caused by the reflected tsunami waves from the Fukushima coast, as described in previous studies. Furthermore, we found that the initial positive wave recorded inside Sendai Bay resulted from the addition of the initial incoming wave and the tsunami wave reflected off Sendai Coast, between Natori River and Sendai Port.

Keywords: The 2016 Fukushima earthquake, Tsunami source inversion, Tsunami numerical modeling

Background

On November 21, 2016 (20:59:49.270 UTC), according to the US Geological Survey (USGS), a normal fault earthquake occurred off the coast of Fukushima, northeast of the Japan Coast. The epicenter estimated bythe Japan Meteorological Agency (JMA) was at 37.392°N, 141.403°S, located approximately 20 km east of the coast of Fukushima Prefecture and 105 km south-east of Sendai Port (Fig. 1a). This event generated a relatively small tsunami that was observed at several tide gauges and offshore stations located along the Pacific North coast of Japan. The JMA issued an initial warning for the coast of Fukushima, with a possible tsunami height of up to 3 m, and a tsunami advisory with heights up to 1 m for other coastal areas, stretching from Aomori Prefecture (north of the epicenter) to Chiba Prefecture (south of the epicenter). Approximately 8 h later, JMA canceled the tsunami warnings and advisories for all areas (Suppasri et al. 2017; Gusman et al. 2017).

Considering that before the 2011 Tohoku Earthquake, the seismic activity on the northern Pacific coast of Japan was relatively low, and since the 2011 event the seismic activity has not also reduced to pre-quake levels, this

*Correspondence: adriano@irides.tohoku.ac.jp
[1] International Research Institute of Disaster Science (IRIDeS), Tohoku University, Aoba 468-1, Aramaki, Aoba-ku, Sendai 980-0845, Japan
Full list of author information is available at the end of the article

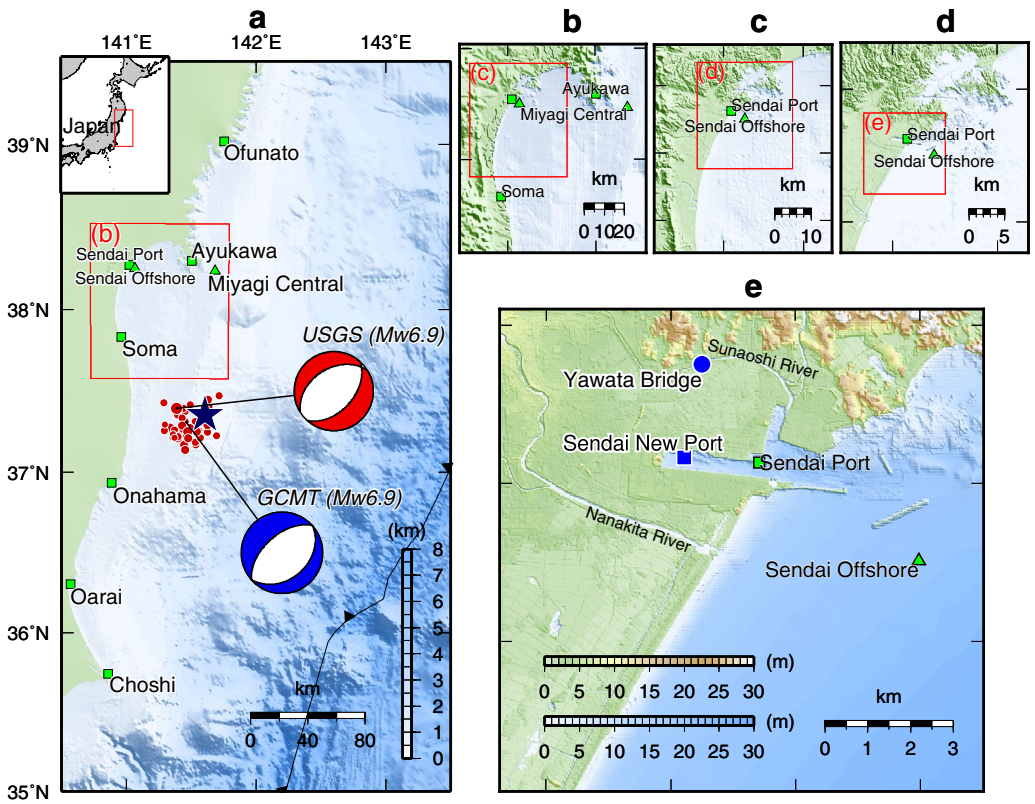

Fig. 1 Location of the wave gauge stations and bathymetry data. **a** The green squares and triangles show the location of the coastal tide gauge and offshore wave gauge stations, respectively. The epicenter of the 2016 Fukushima Earthquake is indicated by the blue star (JMA). Solid and dashed lines indicate the tsunami travel contours in 10- and 5-min intervals, respectively. The focal mechanism is from GCMT and USGS. The red circles show the aftershock distribution within 1 day after the mainshock. Red circles indicate the aftershock distribution within 1 day after the mainshock taken from USGS. **b**–**d** The nested-grid system adopted for the tsunami inundation modeling. **e** The computational domain for the inundation modeling. The blue square shows the location of the tide gauge station of Sendai New Port. The blue circle shows the location of the Yawata bridge, where the water level was measured during the tsunami propagation

earthquake was considered an aftershock of the 2011 Tohoku-Oki Earthquake (Rathi 2016; Aoki and Kikuchi 2016). The moment tensor solution was estimated by several agencies, including the Global CMT Catalog project, the USGS, and the National Research Institute of Earth Science and Disaster Resilience (NIED). All solutions proposed a normal faulting mechanism for this earthquake. The associated moment magnitude, however, differed for each solution. For instance, the GCMT solution estimated a moment magnitude of 3.18×10^{19} Nm ($M_w = 6.9$), with a focal depth at 12.0 km; the USGS's solution estimated a moment magnitude of 2.48×10^{19} Nm ($M_w = 6.90$), with a focal depth at 9.0 km; and the NIED's solution estimated a moment magnitude of 3.47×10^{19} Nm ($M_w = 7.0$; $M_{JMA} = 7.4$), with a focal depth at 11.0 km. The relative differences of the estimated solutions indicates that further studies are needed to better constrain its value. The NIED also evaluated the ground shaking recorded in the strong-motion seismographs network KiK-net and reported a maximum ground pick acceleration (PGA) of 256 cm/s^2 in Iwaki station, Fukushima Prefecture.

The tsunami generated after the 2016 Fukushima earthquake was recorded at several coastal tide gauges and offshore buoys located along the Pacific coast of Japan (Fig. 1a). At stations located south from the epicenter (Onahama, Oarai, and Choshi stations), the maximum tsunami amplitude was recorded during the first cycle of the tsunami waveform; in contrast, the maximum recorded amplitude at almost all stations located north from the epicenter (Miyagi Central, Sendai Offshore, Sendai Port, Ayukawa, and Ofunato) was recorded during the second cycle of the tsunami waveform. The maximum amplitude of the southern stations was 0.6 m (Onahama stations), belonging to the first wave cycle. At the Sendai New Port station, the maximum amplitude was approximately 1.68 m, belonging to the second wave cycle, and the amplitude of the second wave cycle was 0.6

m (Fig. 6). The water level changes due to the intrusion of the generated tsunami into Sunaoshi River was also measured by the river basin monitoring station located close to Yawata bridge (Fig. 1e) (Suppasri et al. 2017).

Tsunami waveform records have been proven to contain reliable information for retrieving the slip distribution of the earthquake source, especially for earthquakes generated along the subduction zones (Satake and Tanioka 1999; Fujii and Satake 2006, 2013; Fujii et al. 2011; Gusman et al. 2015; Heidarzadeh and Satake 2015; Adriano et al. 2016; Yoshimoto et al. 2016). Furthermore, detailed tsunami simulations using high-resolution bathymetry and topography data provide valuable information to specifically analyze tsunami inundation features and thereby validate the estimated tsunami sources (Kakinuma et al. 2012; Fukutani et al. 2016; Adriano et al. 2016; Heidarzadeh et al. 2017). Here, to improve the tsunami source estimate and further analyze the observed tsunami features around Sendai Coast, we first estimate the fault slip distribution of the tsunami source using the moment tensor solution proposed by GCMT and USGS as a reference. We conducted a tsunami waveform inversion analysis of the tsunami signal recorded at seven tide gauges and two wave gauge stations. Finally, the nonlinear tsunami simulation, which uses a finer bathymetry around Sendai Bay, computed from the best fault slip distribution is analyzed to further understand the observed tsunami features around Sendai Coast.

Data

Tsunami waveform data

The generated tsunami was recorded by three tide gauge stations located south of the epicenter, four stations located north of the epicenter, and two offshore wave gauges located north of the epicenter and offshore Sendai Port (Fig. 1a). All stations recorded an initial tsunami wave of negative polarity, which was due to the normal faulting nature of the event (Heidarzadeh et al. 2016). For our waveform inversion analysis, we selected and processed the tsunami data from seven tide gauge stations and two offshore wave gauges (Fig. 1a), considering the small tsunami amplitude observed at stations far from the epicenter. The JMA provided the digital wave signal from the Ofunato, Ayukawa, Sendai, Soma, Onahama, Oarai, and Choshi tide gauge stations. These records have 15-s data sampling durations and include the ocean tide. To obtain the tsunami signal, the ocean tide was approximated to a polynomial function and then removed from the observed records. The tsunami signals at the Miyagi Central and Sendai Offshore wave gauges were published online on the Nationwide Ocean Wave Information Network for Ports and Harbors (NOWPHAS) website; these signals were digitized from the online plots. Finally, all records were resampled to 30-s intervals. An additional tsunami waveform, recorded at the Sendai New Port tide gauge station (Fig. 1b), was digitized from the NOWPAHS website. This latest tide gauge station is located in a narrow bay, approximately 1.8 km in length and 50.0 m in width (Fig. 1d). Due to its location, the tsunami waveform recorded at Sendai New Port station was difficult to reproduce using only linear shallow water equations for the tsunami computation. Thus, this station was not included in the inversion analysis. The stations used for the tsunami waveform inversion are shown in Table 1.

Bathymetry data

All computational domains for nonlinear tsunami modeling are shown in Fig. 1. The grid size varies from 10 to 810 m of spatial resolution. The bathymetry data used in the largest domain (Fig. 1a) are constructed from the 12 arc-s grid interval J-EGG500 (JODC-Expert Grid data for Geography—500 m) published by the Japan Oceanographic Data Center. These data were resampled to construct an 810 m grid size domain. We also combined the local bathymetry data provided by the Miyagi Prefecture office to create the other domains. The grid sizes for domains (b), (c), and (d) are 270, 90, and 30 m, respectively. Finally, the bathymetry data around Sendai Port and Sendai Plain, domain (e) in Fig. 1, were based on 5-m spatial resolution topography and a bathymetry dataset for the period after the 2011 Tohoku tsunami and before the 2016 Fukushima earthquake that was developed by Tohoku University. This dataset also includes two breakwaters located offshore of Sendai Port (Fig. 1e). The final grid size for the last domain is 10 m. For the linear tsunami simulation, an additional computation domain was prepared by merging and resampling all previous five

Table 1 List of stations used for tsunami waveform inversion

Station	Longitude (°E)	Latitude (°N)	Source	A.T. (min.)
Ofunato	141.75	39.02	JMA	49
Ayukawa	141.51	38.30	JMA	35
Sendai Port	141.02	38.27	JMA	63
Sendai Offshore	141.07	38.25	NOWPHAS	57
Miyagi Central	141.68	38.23	NOWPHAS	30
Soma	140.96	37.83	GSI	46
Onahama	140.89	36.93	JMA	29
Oarai	140.57	36.31	JMA	50
Choshi	140.86	35.74	JMA	45

Approximated arrival time estimated from plots of observed tsunami waveforms

JMA Japan Meteorological Agency; *NOWPHAS* Nationwide Ocean Wave Information Network for Ports and Harbors, Japan; *GSI* Geospatial Information Authority of Japan

domains into 3 arc-s of the grid size domain. In this last domain, for proper tsunami modeling at coastal points, the current coastal morphology around Choshi, Oarai, Onahama, Soma, Ayukawa, and Ofunato stations were manually drawn. Here, using the latest satellite images available in Google Earth, we include offshore breakwaters and seawalls that were damaged or destroyed during the 2011 Tohoku tsunami.

Methods

Tsunami numerical modeling

There are two tsunami models used in this study. The first is Tohoku University's numerical analysis model, which was developed to investigate far-field tsunamis and is based on a spherical coordinate system and constant grid (TUNAMI-F1) model (Imamura et al. 1996), and the linear shallow water equations. This model was used to calculate the Green's function in the tsunami waveform inversion analysis. These simulations were computed using the largest domain (Fig. 1a) with a 3 arc-s grid size. The computational time step was set to 0.2 s to satisfy the stability condition, and the total computation time of tsunami propagation was 3 h.

The second tsunami numerical model used is the TUNAMI-N2 version for near-field modeling, which is based on the nonlinear shallow water equations and a Cartesian coordinate system (Imamura et al. 1996). Here, to reduce the computational cost we constructed a nested-grid system, as shown in Fig. 1a–e, of five domains with grid size varying from 10 up to 810 m (Adriano et al. 2016), as described in the previous section. The roughness coefficient was set equal to 0.025 (Kotani et al. 1998) for all computational domains. The computational time step was set to 0.3 s, with a total computation time of tsunami propagation of 6 h. Details of the scheme for nonlinear tsunami modeling are described in Adriano et al. (2013, 2016).

Fault models

Using the observed tsunami arrival time at each station, we first estimate the approximated area for the tsunami source by calculating the back-tsunami projection (inverse travel time) from each station toward the epicenter. The back-tsunami projection was calculated using the Geoware program (GEOWARE 2007). The source area is well constrained by the Onahama and Choshi stations to the south and by the Sendai Offshore and Miyagi Central stations to the north (Fig. 2). The approximate length between Onahama and Miyagi traces is 44 km, which is consistent with the approximated source area of 40.3 km length and 32.3 width (1301.7 km^2) associated with a M_w 6.9 earthquake according to Papazachos et al. (2004)s' scaling law. Thus, we set a tsunami source of 40 km × 32 km (Fig. 2). The assumed fault area is also consistent with the fault area of 1347.8 km^2 given by Murotani et al. (2013).

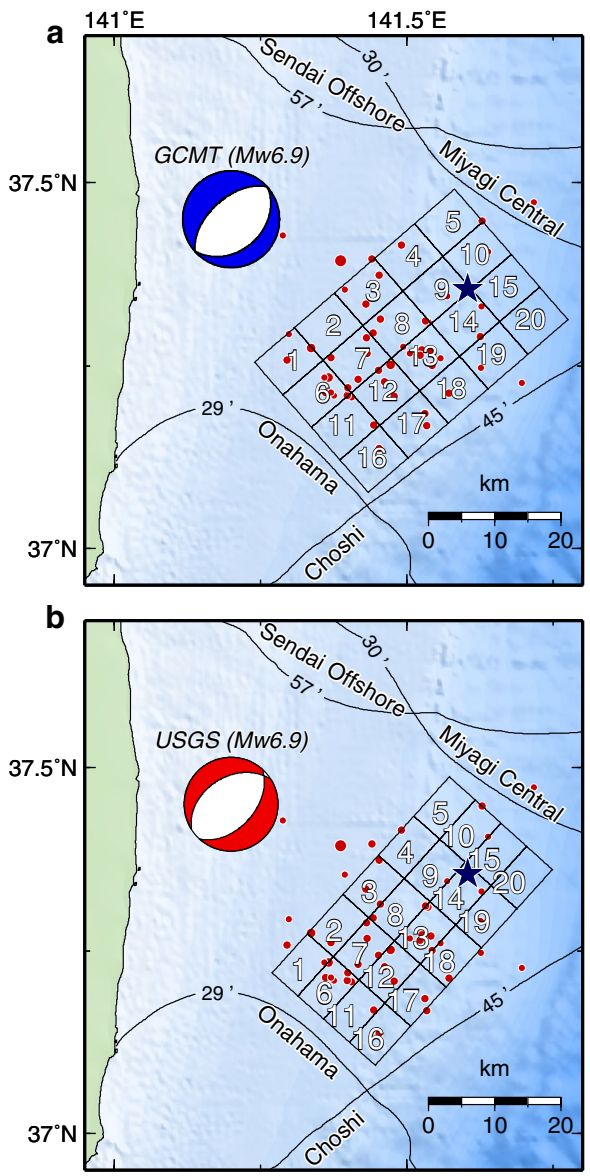

Fig. 2 Fault models. **a** Sub-fault location using the NP1 of GCMT's moment tensor solution. **b** Sub-fault location using the NP2 of USGS's moment tensor solution. Both models are characterized by a southeast deepening direction. The black solid lines show the inverse tsunami travel time from four wave gauge stations toward the source region. The blue star indicates the epicenter. The focal mechanism for each model is from GCMT and USGS. The aftershock distribution (USGS) within 1 day after the main shock are shown by the red circles

At the time of writing this paper, the 2016 Fukushima Earthquake has been investigated by different agencies; as a result, several moment tensor solutions have been associated with this event, including those of the USGS

(WCMT), Global CMT project, NIED (based on F-net system), and JMA (CMT and WCMT). Gusman et al. (2017) conducted a sensitivity analysis of some of the previous solutions by computing synthetic tsunami waveforms based on single-fault models of different dimensions and depths. They found that faults with a 12-km depth better fit the observed tsunami waveform. Furthermore, fault models with southeast deepening direction of the moment solution can reproduce the observed tsunami waveform relatively well. The latest finding can be verified by the post-event survey conducted by the Japan Agency for Marine-Earth Science and Technology (JAMSTEC) around the fault area (available at http://www.jamstec.go.jp/j/about/press_release/20170301/), where 1–2 m recent surface cracks were observed, indicating a northeast–southwest fault orientation.

Here, based on the study conducted by Gusman et al. (2017), we estimated the slip distribution of two fault geometries that are constructed using the nodal plane (NP) of the southeast deepening direction from two different moment tensor solutions. The first model (GCMT) is based on the NP1 from GCMT's solution, with a strike of 49°, dip of 35°, and rake of −89° (Fig. 2a). The second model (USGS) is based on the NP2 from USGS's solution, with a strike of 42°, dip of 49° (Fig. 2b), and rake of −101°. The location of the fault area for each model covers the main area of the aftershock distribution over the span of 1 day. We subdivide the fault area into 20 sub-faults with areas of 8 km × 8 km, with 5 and 4 sub-faults along the strike and dip directions, respectively (Fig. 2a, b). The top depth for each fault model is 1.5 km, which corresponds to sub-faults 1–5. The rest of the depths, from the shallowest to the deepest along the dip direction, are calculated using the corresponding deep angle and the sub-fault's width dimension (Table 2).

Tsunami source inversion

The tsunami waveform inversion analysis is based on the methodology proposed by Satake (1987). This methodology has been proven to be sufficiently powerful to estimate the fault slip distribution of a tsunamigenic earthquake, considering that most of the earthquake source occurs beneath the ocean bottom, particularly in subduction zones (Satake and Tanioka 1999; Fujii and Satake 2006; Adriano et al. 2016; Gusman et al. 2017). We construct the Green's functions using the linear tsunami

Table 2 Fault models and estimated slip for each model

No.	GCMT (NP1)				USGS (NP2)			
	Lon.[a] (°E)	Lat.[a] (°N)	Depth[a] (km)	Slip[a] (m)	Lon.[a] (°E)	Lat.[a] (°N)	Depth[a] (km)	Slip (m)
1	141.24	37.26	1.50	0.00	141.27	37.22	1.50	0.00
2	141.31	37.30	1.50	1.92	141.33	37.27	1.50	2.06
3	141.38	37.35	1.50	1.59	141.39	37.33	1.50	1.66
4	141.44	37.40	1.50	0.70	141.45	37.38	1.50	0.57
5	141.51	37.44	1.50	0.00	141.51	37.43	1.50	0.00
6	141.29	37.21	6.09	0.00	141.31	37.19	7.54	0.22
7	141.36	37.26	6.09	4.66	141.37	37.24	7.54	3.38
8	141.42	37.30	6.09	4.29	141.43	37.30	7.54	5.18
9	141.49	37.35	6.09	0.00	141.50	37.35	7.54	0.00
10	141.56	37.40	6.09	0.38	141.56	37.40	7.54	1.32
11	141.34	37.17	10.68	3.70	141.36	37.16	13.58	4.07
12	141.41	37.21	10.68	0.54	141.42	37.21	13.58	0.00
13	141.47	37.26	10.68	1.39	141.48	37.26	13.58	0.00
14	141.54	37.31	10.68	0.00	141.54	37.32	13.58	0.00
15	141.61	37.35	10.68	0.00	141.60	37.37	13.58	0.00
16	141.39	37.12	15.27	0.21	141.40	37.13	19.61	0.00
17	141.45	37.17	15.27	0.00	141.46	37.18	19.61	0.00
18	141.52	37.22	15.27	0.00	141.52	37.23	19.61	0.00
19	141.59	37.26	15.27	0.00	141.58	37.29	19.61	0.00
20	141.66	37.31	15.27	0.00	141.64	37.34	19.61	0.00

The length and width are 100 km for each sub-fault

[a] Locations (latitude [Lat.], longitude [Lon.], and depth) indicate the westernmost corner of each sub-fault

propagation from each sub-fault, assuming 1 unit slip. The initial seafloor deformation is calculated using a static deformation of a rectangular dislocation model (Okada 1992). In addition, the effect of the co-seismic horizontal displacement, in the region of steep bathymetric slopes (Tanioka and Satake 1996), is included. The tsunami amplitudes recorded at the offshore stations are approximately ten times smaller than those recorded at coastal gauges. To ensure equality on the tsunami amplitudes between the coastal tide gauge stations and the offshore wave gauge stations, a weight factor of 10 was applied to the offshore stations (Fujii et al. 2011). Furthermore, to avoid incorporating nonlinear components from the waveforms at coastal stations, we utilize only the first wave cycle of the synthetic and observed tsunami waveforms. The number of sub-faults satisfies the known–unknown variables condition in the inversion methodology described by Satake (1987). The slip of each sub-fault is estimated using the non-negative least square method, and its corresponding error is calculated using the jackknife method (Fujii and Satake 2006, 2007).

Validation of tsunami source

To evaluate the accuracy of each fault model for reproducing the inundation features around Sendai Port, we conduct nonlinear tsunami simulations using finer bathymetry data with 10 m of spatial resolution. The tsunami waveform recorded at Sendai New Port station, located inside Sendai Bay (Fig. 1e), was used for validation. In addition, the monitoring system of the river basin administered by the Miyagi Prefecture Government recorded the water level at the Sunaoshi River stations (Miyagi Prefecture Government 2016). This station is located near Yawata bridge (Fig. 1e), and the water level was recorded with 1 h of sampling. The first 6 h of the time series of the water level was used to evaluate the accuracy of the fault models. The performance of each fault model on recreating the tsunami data was assessed using the normalized root mean square error (NRMSE) (Heidarzadeh et al. 2016).

Result and discussion

Fault slip distribution

Fault model based on GCMT solution

The largest slips of 4.29–4.66 m are estimated to the southwest of the epicenter, at the shallow depth of 6.09 km (sub-faults 7 and 8). The estimated slip near the surface is 1.92 m in sub-fault 2 and 1.59 in sub-fault 3. A slip of 3.7 m is estimated at a depth of 10.68 km (sub-fault 11). The estimated slip distribution indicates that the rupture propagates southwest of the epicenter, which is also explained by the aftershock distribution (Fig. 3a). The estimated slip for each sub-fault is shown in Table 2. Gusman et al. (2017) suggested a rigidity equal to 2.7×10^{10} N/m^2 based on the shallowest location of the event (Dziewonski and Anderson 1981). Considering the suggested rigidity, the moment magnitude computed from the slip distribution is 3.35×10^{19} Nm (equivalent to $M_w = 6.95$), which is 5% larger than that proposed by GCMT (3.18×10^{19} Nm). The computed seafloor deformation from the slip model generates a maximum subsidence of approximately 1.22 m and uplift of 0.10 m (Fig. 3b). Because of the small dip angle, part of the uplift field is located to the east of the fault area. On the other hand, as described by Gusman et al. (2017), the location and dimension of the subsidence deformation are consistent with underwater 1–2 m surface cracks surveyed by JAMSTEC (Fig. 3c).

In general, the synthetic and observed tsunami waveforms are consistent at most of the stations (Fig. 3c), especially at those located less than 1 arc-degree away from the epicenter. For instance, in the case of Ofunato station (northernmost location) the modeled tsunami arrives slightly slower. The first cycle of the tsunami signal, however, is well reproduced by the slip model. At Ayukawa station, the arrival time, first cycle, and later phases of the tsunami waveform are also generally consistent with the observed data. Although nearly the entire phase of the tsunami signal is relatively well explained at the Sendai Port station, the amplitude of the first negative and positive waves are smaller than the observed ones. In contrast, at the Sendai Offshore and Miyagi Central offshore stations, the synthetic signals are consistent with their corresponding observations. For the Soma, Onahama, and Oarai stations, the first cycle also fits accordingly with the observed data, and the amplitudes are almost perfectly reproduced. The amplitudes in the second cycle, however, are relatively smaller than the recorded data. Finally, the waveform at Choshi station (southernmost location) is not accurately solved by the slip model. Nonetheless, the solutions at these stations are an improvement of previous inversion results (Adriano et al. 2017). The variance reduction obtained from the estimated slip model is approximately equal to 51.5%.

Fault model based on USGS solution

The largest slip of 5.18 m is estimated to the southwest of the epicenter at the shallow depth of 7.54 km (sub-fault 8). The estimated slip near the surface is 2.06 m in sub-fault 2 and 1.66 in sub-fault 3 (Fig. 4a). A slip of 4.07 m is estimated at a depth of 13.58 km (fault 11). The estimated slip for each sub-fault is shown in Table 2. The moment magnitude computed from the slip distribution is 3.17×10^{19} Nm (equivalent to $M_w = 6.94$), assuming a rigidity of 2.7×10^{10} N/m^2. This is 28% greater than the proposed USGS solution (2.48×10^{19}). The computed

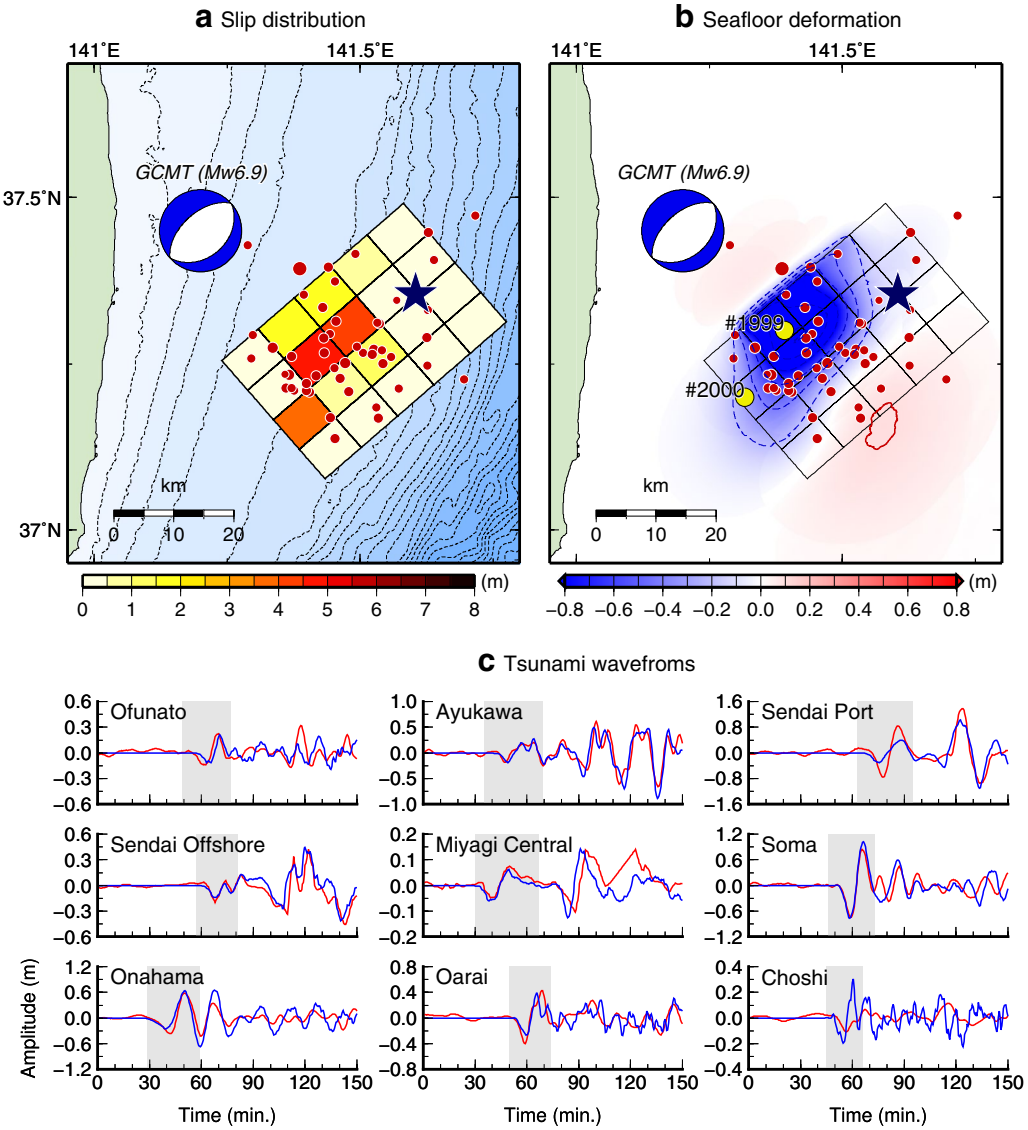

Fig. 3 Inversion result. **a** Estimated slip distribution for the 2016 Fukushima Earthquake based on the GCMT (NP1) fault model. The dashed lines indicate the bathymetry at 30-m depth intervals. **b** Seafloor displacement calculated from the slip distribution. The dashed blue lines indicate the seafloor subsidence in intervals of 0.2 m, and the solid red line indicates seafloor uplift of 0.1 m. Red circles indicate the aftershock distribution within 1 day after the mainshock taken from USGS. The yellow circles indicate the locations of the JAMSTEC survey points, #2000 (37.2°N, 141.32°E) and #1999 (37.3°N, 141.39°E). **c** Comparison of the observed (red lines) and synthetic (blue lines) tsunami waveforms obtained from the estimated slip distribution. The gray areas show the time range used for the inversion

seafloor displacement also generates a larger subsidence of 1.12 m compared with the uplift displacement of 0.19 m (Fig. 4b). The magnitude of the subsidence area generated by this model are also consistent with the underwater surface cracks (1–2 m) found by JAMSTEC (Fig. 4c). Following the behavior of normal faulting events, the uplift region is located to the west of the fault area. This fact may indicate that the USGS model may perform better to reproduce the seafloor deformation due to the 2016 Fukushima tsunami.

The synthetic and observed tsunami waveform are also consistent at most of the stations (Fig. 4c). The synthetic waveform at Ofunato (northernmost location), Ayukawa, Soma, Onahama, and Oarai are well reproduced both in the initial phase and in the later phases, where the first negative and positive amplitudes and the arrival time fit notably well with the observed data. Similarly, at both of the offshore stations (Sendai Offshore and Miyagi Central), the synthetic and observed records are similar. Similar to the previous slip model, the modeled tsunami

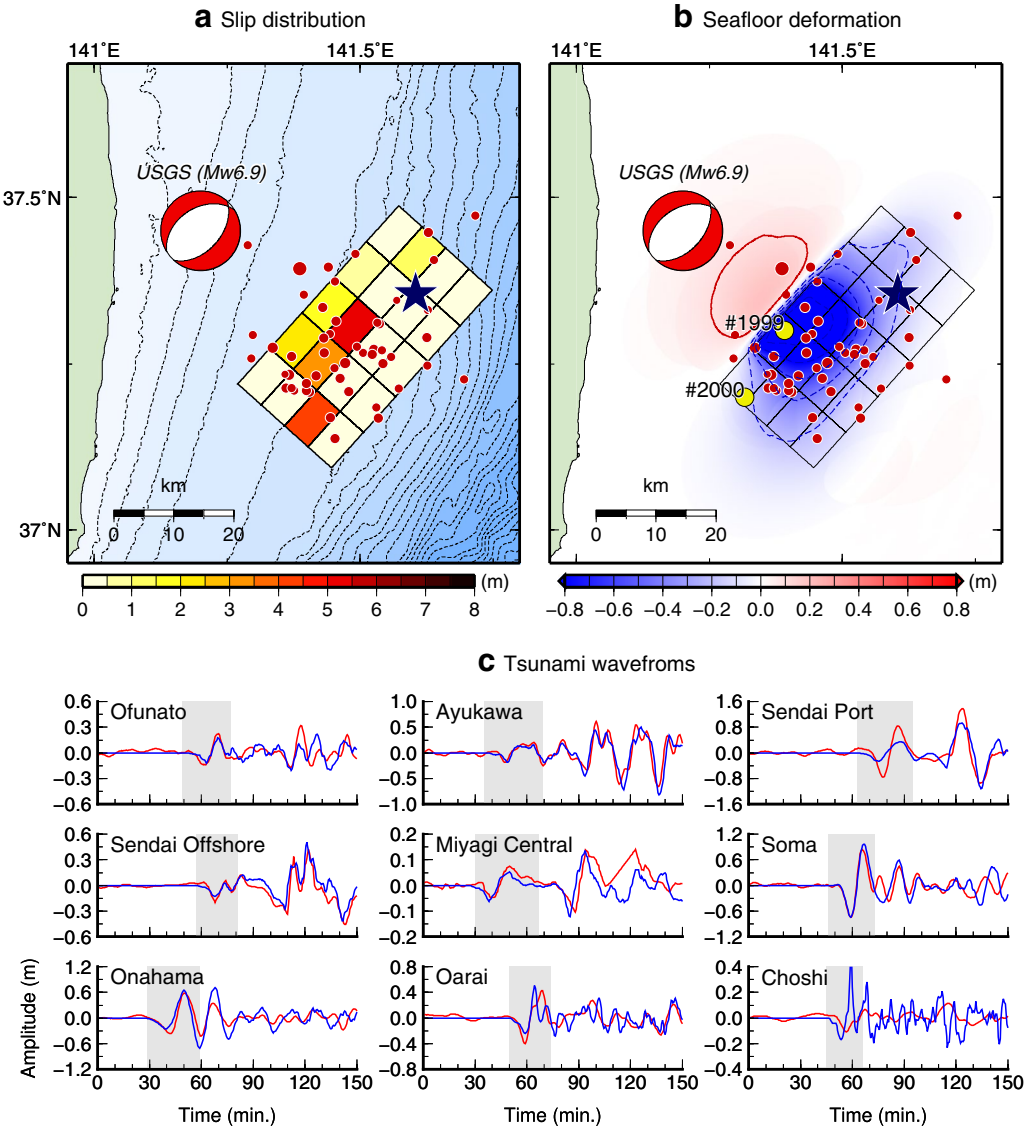

Fig. 4 Inversion result. **a** Estimated slip distribution for the 2016 Fukushima Earthquake based on the USGS (NP2) fault model. The dashed lines indicate the bathymetry in 30-m depth intervals. **b** Seafloor displacement calculated from the slip distribution. The dashed blue lines indicate the seafloor subsidence in intervals of 0.2 m, and the solid red line indicates seafloor uplift of 0.1 m. Red circles indicate the aftershock distribution within 1 day after the mainshock taken from USGS. The yellow circles indicate the locations of the JAMSTEC survey points, #2000 (37.2°N, 141.32°E) and #1999 (37.3°N, 141.39°E). **c** Comparison of the observed (red lines) and synthetic (blue lines) tsunami waveforms obtained from the estimated slip distribution. The gray areas show the time range used for the inversion

signal at the Sendai Port and Choshi stations cannot be well reproduced by the USGS-based slip model. The variance reduction obtained from the estimated slip model is approximately equal to 43.8%.

Comparison of both slip models

In general, the slip distribution from both models shows similar patterns (Figs. 3a, 4a). The largest slip is estimated in the second-shallow fault row, with depths of 6.09 and 7.54 km for the GCMT- and USGS-based fault models, respectively. The slip from the USGS model, however, is almost 1.0 m greater than that from the GMCT model. This is because the depth differs between the sub-faults; in general, deeper sub-faults are associated with greater slip. The former is also observed in the sub-fault at depths of 10.68 and 13.58 km. The associated seafloor deformation also shows similar characteristics in the subsidence regions, with maximum displacements of approximately

1.20 m for both models. The uplift region, however, is located at different sections of the fault area (Figs. 3b, 4b); i.e., east in the GCMT model and west in the USGS model. These conditions are related to the dip angle, as steep angles generate the highest vertical displacement and gradual faults lead to expanded deformation (Satake and Tanioka 1999; Tanioka and Satake 1996). The small dip angle of the GCMT slip model generates an uplift field on the hanging wall (east of the fault plane).

Comparison of tsunami features at Sendai Bay

Figure 5 shows snapshots (70, 90, 110, and 130 min) of tsunami propagation from both slip models. As expected, the negative tsunami height, from both models, arrives first at Sendai Port. In both cases, the tsunami propagates with similar characteristics during approximately the first 90 min (Fig. 5). However, after approximately 110 min, the tsunami propagation from the USGS model is slightly delayed with respect to the GCMT model. This is clearly observed after 130 min of propagation, where the second positive tsunami wave in the GCMT model has already entered Sendai Bay and moves towards Yawata bridge, along the Sunaoshi River. Conversely, the positive wave from the USGS model enters Sendai Bay. Figure 6 shows the synthetic comparison from both modes and the recorded tsunami height at the Sendai New Port tide gauge station, which is located inside Sendai Bay (Fig. 1). Both models generally agree well with the observed data, especially in terms of the phase of the first and second waves. We calculate the NRMSE and observe that the GCMT performed better because it fits well with the observed data at the Sendai New Port station. The NRMSE are 0.686 and 0.863 and the GCMT and USGS models, respectively.

The estimated water levels at the Sunaoshi River station (Yawata bridge) from both models are shown in Fig. 7. Although the computed water levels form both models are fairly consistent for the first 2 h, both models underestimated the observed data after 2 h of inundation. In addition, our tsunami simulation does not take into account the river flow from the mountain, which may cause the underestimation of the observed data. The maximum observed water level was 0.7 m (above the normal level), and it occurred at approximately 3 h of tsunami intrusion into the river, as reported by Suppasri et al. (2017).

Analysis of the tsunami propagation around Sendai Bay

The propagation along Sendai Coast (Fig. 8) shows that during the initial cycle, with negative polarity, the waves first hit the coastal area south of the Soma station

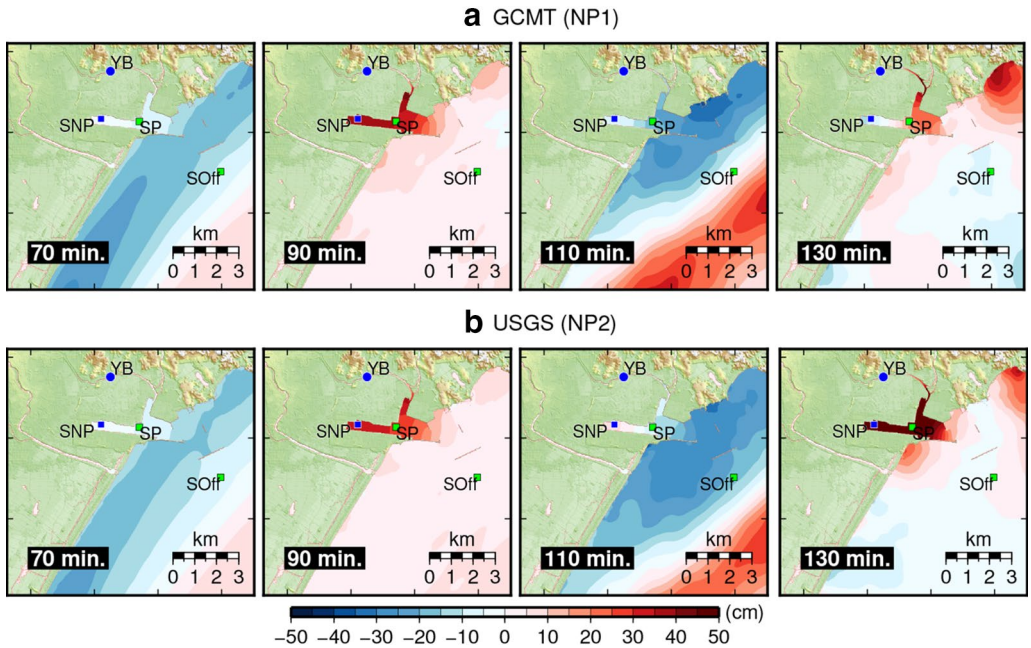

Fig. 5 Tsunami propagation around Sendai Port. **a** Snapshot of the tsunami propagation computed from the GCMT slip model. **b** Snapshot of the tsunami propagation computed from the USGS slip model. The tsunami heights in both models are plotted at the same scale and are indicated by the color-scale bar. Notation for all panels: *SNP* Sendai New Port station; *SP* Sendai Port station; *SOff* Sendai Offshore stations; *YB* Yawata bridge

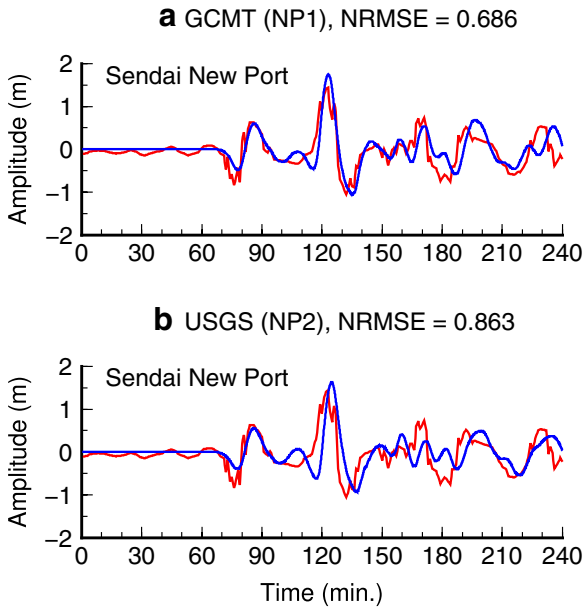

Fig. 6 Tsunami signal at Sendai New Port station. **a** Comparison between the observed (red line) and synthetic tsunami waveform (blue line) computed from the GCMT slip model. **b** Comparison between the observed (red line) and synthetic tsunami waveform (blue line) computed from the USGS slip model

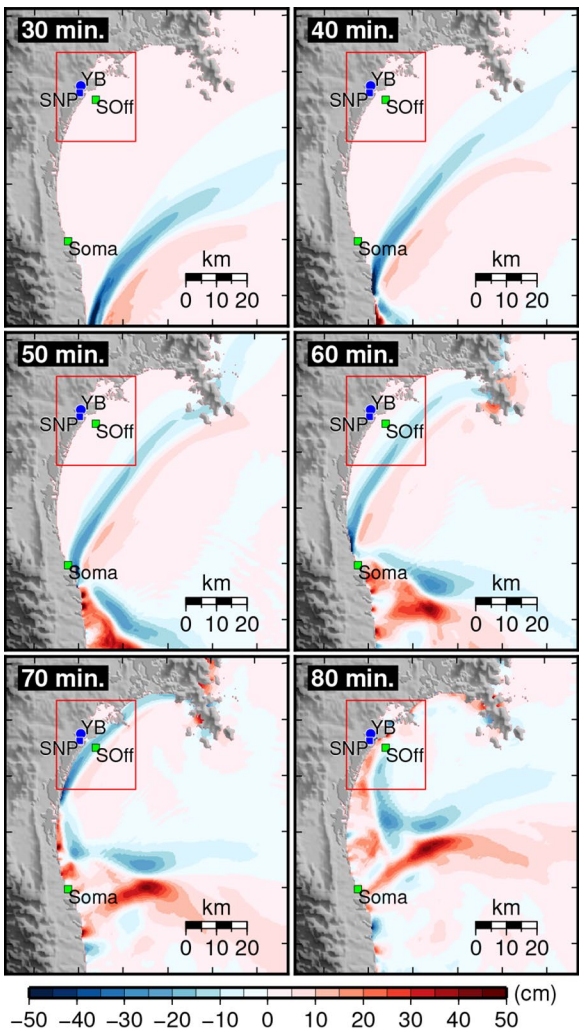

Fig. 8 Tsunami propagation along Sendai coast. Snapshot of the tsunami height propagation computed from the GCMT slip model. The red square shows the area shown in Fig. 9

approximately 30 min after the mainshock. Then, after 50 min of propagation, most of the tsunami wave was reflected towards Sendai Coast, exhibiting a tsunami height of approximately 0.5 m after 80 min of propagation. This phenomenon created a secondary cycle, with positive polarity, that was responsible for the high tsunami amplitude recorded at tide gauge stations located north of Soma Coast (Miyagi Central, Sendai Offshore, Sendai Port, and Sendai New Port stations). For instance,

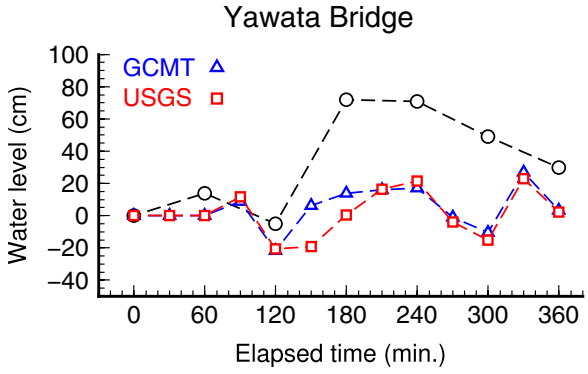

Fig. 7 Water level recorded at Sunaoshi station. The circles show the water level measured around Yawata bridge within the first 6 h. The triangles and squares show the computed waver level at 30-min intervals from the GCMT and USGS slip models, respectively

the maximum tsunami amplitude observed at Sendai New Port station was approximately 1.7 m, which corresponds to the second cycle that arrived at approximately 120 min of tsunami propagation. This characteristic in the tsunami waveform was also reported by Gusman et al. (2017) and Suppasri et al. (2017). This tsunami did not produce substantial inland inundation; however, a close look at the tsunami propagation over Sendai Port (Fig. 9) reveals that after the first negative wave hit and entered into Sendai Port, approximately 70 min after the mainshock, the following positive wave hit the coastal area between the Naroti River and Sendai Bay (80 min after the mainshock, Fig. 9). This wave then was reflected between the coastline and the continental shelf in this area producing additional wave systems (Yamazaki 2011) that partially entered into Sendai Bay (90 min after the

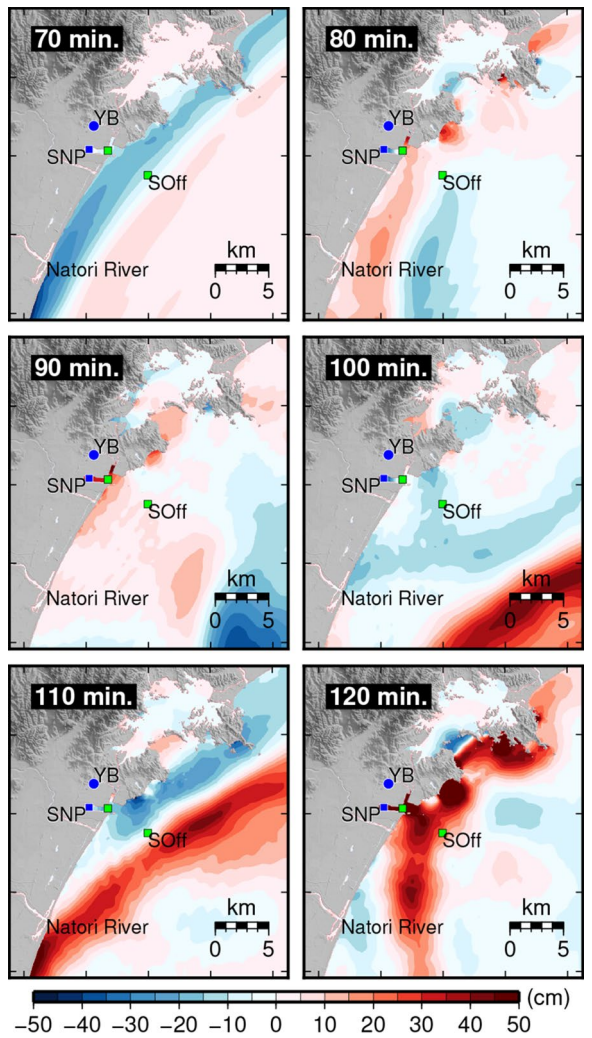

Fig. 9 Tsunami propagation along Sendai Port. Snapshot of the tsunami height propagation computed from the GCMT slip model

mainshock), which may have also been responsible for the initial 0.7 m tsunami amplitude recorded at the Sendai New Port station. Our simulation also shows that the reflected wave from Soma Coast approached the Sendai Offshore station after 110 min of tsunami propagation with an amplitude of approximately 0.5 m.

Conclusion

We estimated the tsunami source of the 2016 Fukushima Earthquake, adopting two fault geometries based on the GCMT and the USGS moment tensor solutions. The slip distribution from both models was estimated using the tsunami signal recorded at seven tide gauge stations and two offshore wave gauges located on the north Pacific coast of Japan. We found that although both slip models could solve the recorded tsunami waveforms relatively well, the GCMT-based slip model (strike = 49°, dip = 35°, and rake = −89°) better explained the observed data at most of the stations. This slip model also accurately solved the later wave phases of the tsunami waveform that were not used for the waveform inversion. The inversion result yielded a fault with an area of 40 km × 332 km extending southwest from the epicenter. The largest slip was estimated as 4.66 m at 6.09 km depth, while larger slips also concentrated between 6.06 and 10.68 km depth, located southwest of the epicenter. Assuming a rigidity of 2.7×10^{10} N/m^2, the moment magnitude computed from the GCMT slip model was 3.35×10^{19} Nm (equivalent to $M_w = 6.95$), which is slightly larger than that proposed by GCMT (3.18×10^{19} Nm). Using both slip models, we conducted a nonlinear tsunami simulation using high-resolution bathymetry data to analyze the tsunami propagation around Sendai Coast. It was found that the GCMT slip model accurately reproduced the tsunami waveform recorded at Sendai New Port (NRMSE = 0.686). The nonlinear simulation using the GCMT slip model also precisely reproduced the arrival time and amplitude of the second positive wave recorded inside Sendai Bay (amplitude = 1.65 m). The simulation using finer bathymetry data also verified the previous findings, which stated that the secondary positive wave, as observed at the station located north of the epicenter, was due to the reflection of the initial tsunami wave (negative polarity) after impacting the coastal region of Soma city. Finally, our simulations also highlight that the initial positive wave recorded inside Sendai Bay was the result of the addition of the initial incoming wave and the reflected tsunami wave from Sendai Coast, between Natori River and Sendai Port.

Authors' contributions

BA conducted the data analysis and solutions, and wrote the major portion of the manuscript. YF and SK supervised the proceeding of the analysis, and helped writing the manuscript. All have substantial contributions to the completion of the study. All authors read and approved the final manuscript.

Author details

[1] International Research Institute of Disaster Science (IRIDeS), Tohoku University, Aoba 468-1, Aramaki, Aoba-ku, Sendai 980-0845, Japan. [2] International S (IISEE), Building Research Institute (BRI), 1 Tachihara, Tsukuba, Ibaraki, Tsukuba 305-0802, Japan.

Acknowledgements

This research was supported by the Japan Society for the Promotion of Science (JSPS) under the Project: Fusion of Real-time Simulation and Remote Sensing for Tsunami Damage Estimation to Latin America (JSPS-Grant: P16055), the JST CREST (Grant number JPMJCR1411), and the Ministry of Education, Culture, Sports, Science and Technology (MEXT) of JAPAN.

Competing interests

The authors declare that they have no competing interests.

Consent for publication

Not applicable.

Ethical approval and consent to participate
Not applicable.

Publisher's Note

Received: 12 September 2017 Accepted: 29 December 2017
Published online: 12 January 2018

References

Adriano B, Mas E, Koshimura S, Fujii Y, Yauri S, Jimenez C, Yanagisawa H (2013) Tsunami inundation mapping in Lima, for two tsunami source scenarios. J Disaster Res 8(2):274–284. https://doi.org/10.20965/jdr.2013.p0274

Adriano B, Mas E, Koshimura S, Fujii Y, Yanagisawa H, Estrada M (2016) Tsunamis and earthquakes in coastal environments. Coastal research library, 14th edn. Springer, Cham, pp 1–16. https://doi.org/10.1007/978-3-319-28528-3

Adriano B, Hayashi S, Gokon H, Mas E, Koshimura S (2016) Understanding the extreme tsunami inundation in Onagawa town by the 2011 Tohoku earthquake, its effects in urban structures and coastal facilities. Coast Eng J 58(4):1640013. https://doi.org/10.1142/S0578563416400131

Adriano B, Furuya T, Mas E, Koshimura S (2017) Tsunami source of the M_w 7 2016 Fukushima earthquake inferred from tide gauge and GPS buoy records. In: JpGU-AGU joint meeting 2017. May 20–25, Chiba, Japan, p 12

Aoki M, Kikuchi D (2016) M.7.4 quake was triggered by vertical split in undersea rock: experts. http://www.japantimes.co.jp/news/2016/11/22/national/m-7-4-quake-triggered-vertical-split-undersea-rock-experts/#.WVszmcaB1dC. Accessed 6 June 2017

Dziewonski AM, Anderson DL (1981) Preliminary reference Earth model. Phys Earth Planet Inter 25(4):297–356. https://doi.org/10.1016/0031-9201(81)90046-7

Fujii Y, Satake K (2006) Source of the July 2006 West Java tsunami estimated from tide gauge records. Geophys Res Lett 33(24):1–5. https://doi.org/10.1029/2006GL028049

Fujii Y, Satake K (2007) Tsunami source of the 2004 Sumatra-Andaman earthquake inferred from tide gauge and satellite data. Bull Seismol Soc Am 97(1A):192–207. https://doi.org/10.1785/0120050613

Fujii Y, Satake K (2013) Slip distribution and seismic moment of the 2010 and 1960 Chilean earthquakes inferred from tsunami waveforms and coastal geodetic data. Pure Appl Geophys 170(9–10):1493–1509. https://doi.org/10.1007/s00024-012-0524-2

Fujii Y, Satake K, Sakai S, Shinohara M, Kanazawa T (2011) Tsunami source of the 2011 off the Pacific coast of Tohoku Earthquake. Earth Planets Space 63(7):815–820. https://doi.org/10.5047/eps.2011.06.010

Fukutani Y, Anawat S, Imamura F (2016) Uncertainty in tsunami wave heights and arrival times caused by the rupture velocity in the strike direction of large earthquakes. Nat Hazards 80(3):1749–1782. https://doi.org/10.1007/s11069-015-2030-1

GEOWARE (2007) The tsunami travel times (TTT). http://www.geoware-online.com/tsunami.html. Accessed 6 June 2017

Gusman AR, Murotani S, Satake K, Heidarzadeh M, Gunawan E, Watada S, Schurr B (2015) Fault slip distribution of the 2014 Iquique, Chile, earthquake estimated from ocean-wide tsunami waveforms and GPS data. Geophys Res Lett 42(4):1053–1060. https://doi.org/10.1002/2014GL062604

Gusman AR, Satake K, Shinohara M, Sakai S, Tanioka Y (2017) Fault slip distribution of the 2016 Fukushima earthquake estimated from tsunami waveforms. Pure Appl Geophys 174(8):2925–2943. https://doi.org/10.1007/s00024-017-1590-2

Heidarzadeh M, Satake K (2015) New insights into the source of the Makran tsunami of 27 November 1945 from tsunami waveforms and coastal deformation data. Pure Appl Geophys 172(3–4):621–640. https://doi.org/10.1007/s00024-014-0948-y

Heidarzadeh M, Harada T, Satake K, Ishibe T, Gusman AR (2016) Comparative study of two tsunamigenic earthquakes in the Solomon islands: 2015 M w 7.0 normal-fault and 2013 Santa Cruz M w 8.0 megathrust earthquakes. Geophys Res Lett 43(9):4340–4349. https://doi.org/10.1002/2016GL068601

Heidarzadeh M, Murotani S, Satake K, Ishibe T, Gusman AR (2016) Source model of the 16 September 2015 Illapel, Chile, M w 8.4 earthquake based on teleseismic and tsunami data. Geophys Res Lett 43(2):643–650. https://doi.org/10.1002/2015GL067297

Heidarzadeh M, Murotani S, Satake K, Takagawa T, Saito T (2017) Fault size and depth extent of the Ecuador earthquake (M w 7.8) of 16 April 2016 from teleseismic and tsunami data. Geophys Res Lett 44(5):2211–2219. https://doi.org/10.1002/2017GL072545

Imamura F (1996) Review of the tsunami simulation with a finite difference method. In: Yeh H, Liu P, Synolakis C (eds) Long wave run-up models. World Scientific, Singapore, pp 25–42

Kakinuma T, Tsujimoto G, Yasuda T, Tamada T (2012) Trace survey of the 2011 Tohoku tsunami in the north of Miyagi Prefecture and numerical simulation of bidirectional tsunamis in Utatsusaki Peninsula. Coast Eng J 54(1):1250007. https://doi.org/10.1142/S0578563412500076

Kotani M, Imamura F, Shuto N (1998) Tsunami run-up simulation and damage estimation by using GIS. In: Proceedings coastal engineering JSCE45, pp 356–360

Miyagi Prefecture Government (2016) Monitoring system of the river basin, Sunaoshi river water level. http://www.dobokusougou.pref.miyagi.jp/miyagi/servlet/Gamen1Servlet

Murotani S, Satake K, Fujii Y (2013) Scaling relations of seismic moment, rupture area, average slip, and asperity size for M ~9 subduction-zone earthquakes. Geophys Res Lett 40(19):5070–5074. https://doi.org/10.1002/grl.50976

Okada Y (1992) Internal deformation due to shear and tensile faults in a half-space. Bull Seismol Soc Am 82(2):1018–1040

Papazachos BC, Scordilis EM, Panagiotopoulos DG, Karakaisis GF (2004) Global Relations between seismic fault parameters and moment magnitude of earthquakes. In: The 10th international Congress. Thessaloniki, vol XXXVI, pp 1482–1489

Rathi A (2016) The latest earthquake in Japan was an aftershock of the one five years ago. https://qz.com/843697/the-magnitude-6-9-earthquake-near-fukushima-was-an-aftershock-of-the-devastating-2011-earthquake/. Accessed 6 June 2017

Satake K (1987) Inversion of tsunami waveforms for the estimation of a fault heterogeneity: method and numerical experiments. J Phys Earth 35:241–254

Satake K, Tanioka Y (1999) Sources of tsunami and tsunamigenic earthquakes in subduction zones. Pure Appl Geophys 154(3–4):467–483. https://doi.org/10.1007/s000240050240

Suppasri A, Leelawat N, Latcharote P, Roeber V, Yamashita K, Hayashi A, Ohira H, Fukui K, Hisamatsu A, Nguyen D, Imamura F (2017) The 2016 Fukushima earthquake and tsunami: local tsunami behavior and recommendations for tsunami disaster risk reduction. Int J Disaster Risk Reduct 21(January):323–330. https://doi.org/10.1016/j.ijdrr.2016.12.016

Tanioka Y, Satake K (1996) Tsunami generation by horizontal displacement of ocean bottom. Geophys Res Lett 23(8):861. https://doi.org/10.1029/96GL00736

Yamazaki Y, Cheung KF (2011) Shelf resonance and impact of near-field tsunami generated by the 2010 Chile earthquake. Geophys Res Lett. https://doi.org/10.1029/2011GL047508

Yoshimoto M, Watada S, Fujii Y, Satake K (2016) Source estimate and tsunami forecast from far-field deep-ocean tsunami waveforms—the 27 February 2010 *Mw* 8.8 Maule earthquake. Geophys Res Lett 43(2):659–665. https://doi.org/10.1002/2015GL067181